



# Geomorphology and structural development of the nested summit crater of Láscar Volcano studied with Terrestrial Laser Scanner data and analogue modelling



Elske de Zeeuw-van Dalfsen<sup>a,\*</sup>, Nicole Richter<sup>a</sup>, Gabriel González<sup>b</sup>, Thomas R. Walter<sup>a</sup>

<sup>a</sup>GFZ - German Research Center for Geosciences, Telegrafenberg, Potsdam, Germany

<sup>b</sup>National Research Center for Integrated Natural Disaster Management, Universidad Católica del Norte, Antofagasta, Chile

## ARTICLE INFO

### Article history:

Received 9 March 2016

Received in revised form 15 September 2016

Accepted 21 September 2016

Available online 24 September 2016

### Keywords:

Láscar Volcano

Terrestrial Laser Scanner (TLS)

Geomorphology

Nested craters

Sandbox modelling

## ABSTRACT

Many volcano summits host craters that are partially overlapping. The formation of such nested craters has been commonly interpreted as vent migration. Here, we present an additional mechanism that may explain the geometry of nested craters at volcanoes. Láscar Volcano, the most active volcano of the Central Volcanic Zone in the Chilean Andes, hosts ENE-WSW trending summit craters that are partially overlapping (nested). Details on the evolution and interaction between the different craters remain unclear.

To create a robust dataset, Terrestrial Laser Scanner (TLS) data were collected at the summit of Láscar in 2013. The resulting topographic data set, consisting of more than 15 million data points with centimetre sampling, allows visualising almost the complete eastern edifice of the volcano's summit. From the TLS data, a Digital Elevation Model (DEM) and a slope map were generated allowing us to create a lineament map and quantify the observed morphological and structural features. To further improve our understanding of the processes responsible for the formation of the craters and geomorphology, we designed sandbox analogue models. Results suggest that one of the craters is a 'parasite' crater, formed as a consequence of ongoing activity in the adjacent crater. Our data suggest that the nested craters have all been modified since the last major eruption in 1993, by near surface effects associated with cooling, compaction and gravitational sliding of the crater floor infill. As the active crater deepens, the adjacent inactive crater extends and partially slumps towards the active one. Understanding the structural development of these nested craters is relevant for assessing potential future eruption sites, thus making Láscar a dynamic target for a detailed morphology study. These findings may similarly be applied to other volcanoes, where nested craters have developed.

© 2016 Elsevier B.V. All rights reserved.

## 1. Introduction

Volcanic craters are steep-sided, bowl- or funnel-shaped, depressions of less than 1 km across, formed by either explosion or collapse and often located at the top of a volcanic cone (Lipman, 2000). One classification, based on genesis (Jagger, 1947), distinguishes three crater types: *i*) Concentric construction craters, *ii*) Explosion craters and *iii*) Engulfment craters. Concentric construction craters develop when material that is thrown out forms a ridge exhibiting concentric inward and outward slopes (Jagger, 1947). Explosion craters form when, during an eruption, a basin is created by erosion and/or excavation (Valentine et al., 2012). Engulfment or pit craters form by collapse mechanisms (Holohan et al., 2011; Roche et al., 2001) often associated with depletion of magma below the crater floor (Jagger, 1947).

Many summit craters have a nested appearance, such as at Santa Ana in El Salvador (Scolamacchia et al., 2010), Masaya in Nicaragua (Rymer et al., 1998), El Misti in Peru (Thouret et al., 2001) and Láscar in Chile (Gardeweg et al., 1998). However, processes responsible for the nested architecture are often poorly understood. In general, both explosion and collapse related nested craters are thought to be associated with a migration of the eruption vent and/or the underlying reservoir (Lipman, 1997).

Even though in this work we focus on nested crater architectures, other volcanic features, such as cones or calderas can also appear nested. Partially overlapping architectures can be formed by an underlying magma-feeding fracture, feeding multiple eruption points, such as at several of the parasitic cones of Mount Etna in Italy (Corazzato and Tibaldi, 2006). On a different scale, calderas (> 1 km in diameter) can also appear nested, e.g. at Campi Flegrei in Italy (Acocella, 2008) and at Mauna Loa, Hawai'i (Lockwood, 1990). In the Central Andes, nested calderas of the Altiplano-Puna volcanic complex, have been described by de Silva (1989).

\* Corresponding author.

Láscar Volcano ( $23^{\circ} 22' S$   $67^{\circ} 44' W$ , Fig. 1a), located in the Chilean Andes 70 km SE of San Pedro de Atacama, is the most active volcano of the Central Volcanic Zone (CVZ). Today the volcanic complex consists of the dormant western edifice and the active eastern edifice (Fig. 1c), the latter comprising three overlapping craters (Fig. 1d). The volcanic complex experienced several major, up to VEI 6, pre-historic eruptions (Gardeweg et al., 1998) but no calderas were formed. The three craters of the eastern edifice formed unrelated to any large explosive events, as no evidence exists for a deposit witnessing such an explosion (Gardeweg et al., 1998). Finally, the last major (VEI 4) eruption of 1993 did not change the crater morphology of the eastern craters extensively (Denniss et al., 1998). Therefore Matthews et al. (1997) suggested the nested craters of Láscar did not form due to a large explosion nor due to simple collapse but rather as a result of long term cyclic activity: dome growth, followed by degassing of a shallow magma reservoir and conduit, resulting in subsidence of the dome and further deepening of the crater floor.

The details of the formation of nested craters might be better understood based on geomorphological and structural data obtained by high precision topographic mapping. Such datasets can be acquired by e.g. satellite, airborne and close-range photogrammetry, by radar, by Airborne Laser Scanning (ALS) or by Terrestrial Laser Scanning (TLS). The biggest advantage of TLS data is the ability to acquire topographic data of very high quality and spatial resolution in relatively little time. Thanks to its portability, TLS data can be acquired even at very high altitude volcano peaks, when the location is accessible and viewing geometries are favourable. Furthermore, the results allow direct quantitative measurements of observations in a local reference frame. In volcanology, TLS has successfully been used to study lava flow morphology (James et al., 2009), landslides (Jones et al., 2009) and the geometry of eruption conduits (Geyer et al., 2015; LaFemina et al., 2015). In Chile, TLS was used at volcanoes to study pyroclastic flow deposits (Jessop et al., 2012). The morphology of active craters has been studied with TLS for example

at Erebus, Antarctica (Jones et al., 2015) and at Vesuvius (Pesci et al., 2011) and Vulcano (Pesci et al., 2013) in Italy. The use of repeated TLS allows e.g. to monitor the spatial-temporal changes in the ground deformation of an active crater (Pesci et al., 2011) and the lava lake levels (Jones et al., 2015).

To better understand the formation and structural architecture of craters, analogue model experiments have been used (Roche et al., 2001; Valentine et al., 2012). A systematic series of sandbox models can provide insights into the geometric, dynamic and/or kinematic evolution of volcanic craters and thus help to reveal processes or structures that can not (easily) be observed in nature. Most analogue model studies have however focussed on caldera evolution. These studies simulated a buried draining reservoir to identify caldera collapse structures (Branney, 1995; Komuro, 1987; Marti et al., 1994). To study specific cases and to investigate more specific parameters of caldera collapse processes, further improvements and/or changes to the model set-ups were made by different authors (Acocella et al., 2001; Holohan et al., 2008; Kennedy et al., 2008; Poppe et al., 2014; Walter and Troll, 2001).

Here, we study the structural pattern of the nested craters of Láscar in unprecedented detail using TLS and sandbox modelling. In order to better understand the formation, development and stability of the nested craters of Láscar, we measure the topography of the sandbox craters and compare the findings to the real craters of Láscar. We evaluate and examine the morphological features observed and we discuss the most likely process responsible for the nested crater evolution.

## 2. Study area

The Central Volcanic Zone (CVZ) is a surface expression of the subduction of the Nazca plate (Fig. 1a) beneath the western margin of the continental South American plate. Regional ignimbrite producing

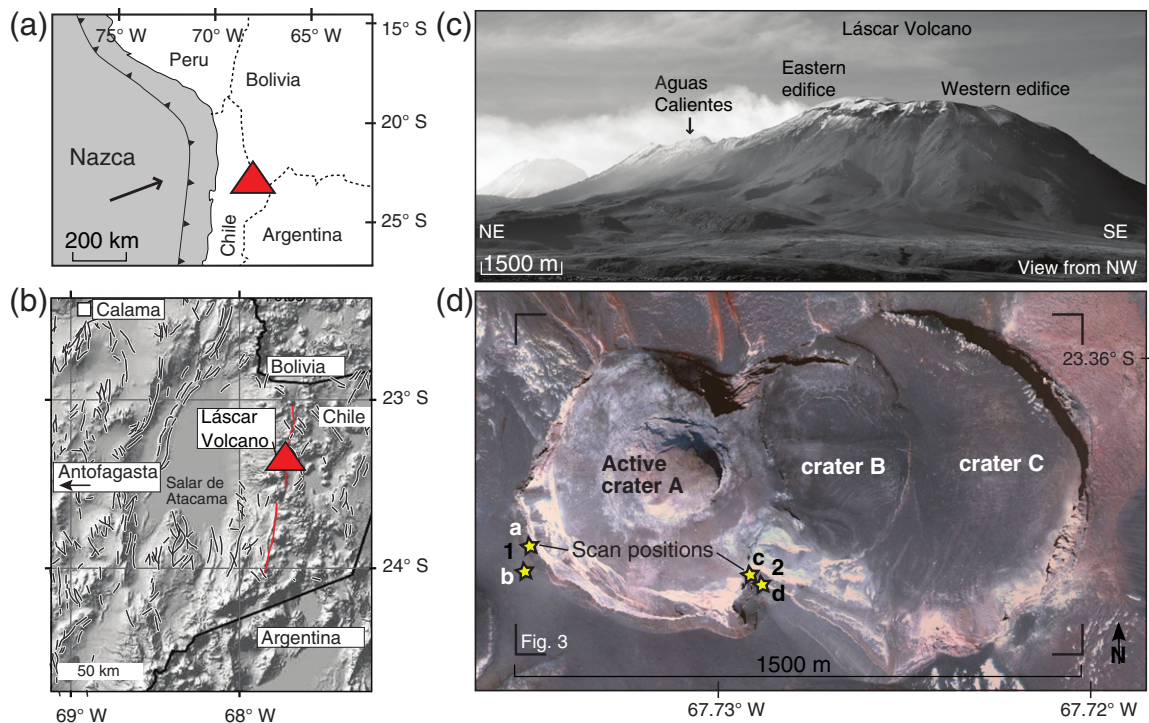


**Fig. 1.** a) Location of Láscar Volcano (red triangle) in Chile, South-America (N is up). The subduction trench of the Nazca Plate is shown. b) Close up of the setting of Láscar Volcano (N is up) showing tectonic faults (black lines) and the N-S Miscanti fault (red line) underlying the volcano. c) Photo of the active edifice as well as the dormant western edifice of Láscar Volcano and the neighbouring Aguas Calientes Volcano. d) Google Earth image of 12 September 2008, showing the three craters of the edifice and the scan locations (yellow stars).

volcanism within the CVZ, in the late Miocene, resulted in the formation of the Altiplano-Puna Volcanic Complex (APVC), a large silicic volcanic-tectonic province located between lat 21° and 24° S. Prominent volcanoes within this complex are Uturuncu, Láscar, Putana and Cerro Blanco Caldera. Láscar Volcano is a highly active, 5592 m high, composite stratocone located in the southwestern part of the APVC (de Silva, 1989; de Silva et al., 2006). A several km-long, N-S-trending lineament, the 'Miscanti fault', cuts the Quaternary volcanic deposits underlying the Láscar Volcano (González et al., 2009; Zellmer et al., 2014) (Fig. 1b).

The pre-historic evolution of Láscar can be divided in four stages (Gardeweg et al., 1998). During stage I (43–26.5 ka), a mafic-andesitic stratocone formed. Activity then switched to West, where during stage II (26.5 ka) a silicic lava dome complex formed, culminating with the Soncor ignimbrite eruption (Gardeweg et al., 1998; Matthews et al., 1997). During stage III (22.3 ka–ca. 9.3 ka), a dacite-andesite stratocone formed on top of the existing edifice. Two summit craters, which are still visible today in the dormant western edifice, were formed during the Tumbres eruption (Gardeweg et al., 1998) around 9.3 ka ago. Finally, activity switched back to the eastern edifice, where, during stage IV (<9.3 ka), three nested summit craters were formed.

The three nested summit craters become younger towards the West (Matthews et al., 1997), implying a westward migration of the centre of activity. We name the craters, from West to East: crater A, crater B and crater C; crater A being the currently active one (Fig. 1d). Their formation was not associated with any recognised large pyroclastic summit eruption, nor did any flank or parasitic eruptions occur during stage IV. Therefore, Matthews et al. (1997) suggest a cyclic eruption process formed the initial craters rather than a caldera-like collapse. Each cycle starts with lava dome extrusion and degassing at fumaroles. Withdrawal of magma into the deep chamber and degassing of the system leads to subsidence of the dome and crater floor, facilitated by inward-dipping fractures reminiscent of a funnel. Gas pressure builds up as magma and host rock become increasingly impermeable, ending the cycle with an eruption. This recurrent process ultimately resulted in the subsidence of the crater floor and is the proposed mechanism for the initial formation of the three steep-walled, circular craters (Matthews et al., 1997).

Since the last major (VEI 4) eruption in 1993, Láscar has had 10 minor eruptions, most recently in April 2013 and October 2015. During the 1993 eruption, pyroclastic flows covered 18.5 km<sup>2</sup> and the ash column reached up to 22 km altitude (Denniss et al., 1998). No volcano wide surface deformation, governing the 1993 eruption, was identified (Pritchard and Simons, 2002, 2004), implying that no major shallow magma reservoir was evacuated. Other studies at Láscar have focussed on pyroclastic flow deposits (Calder et al., 2000; Jessop et al., 2012; Sparks et al., 1997), the region's subsurface electrical conductivity (Diaz et al., 2012) and degassing of the active craters (Tassi et al., 2009). Thermal anomalies were identified prior to and during the recent eruptions (Francis and de Silva, 1989; Glaze et al., 1989; Oppenheimer et al., 1993). Pavez et al. (2006) showed that small-scale subsidence could be observed in crater B, over a two-month period in 1995. They suggest this episode of crater floor subsidence originates from a conduit-related process below this crater. According to their findings, the removal of magmatic fluids (upraised magma or gas) subsequent to the July 1995 eruption, produced a pressure release at subsurface levels, leading to a moderate crater floor collapse. The alternative explanation for the subsidence was the reactivation of a post-1993-eruption fracture, crossing crater B (Pavez et al., 2006). However, the reason why crater B deforms, although all historical eruptive activity takes place only at crater A, remains unclear. The high ongoing activity and the intriguing architecture of the nested summit craters make Láscar an exemplary case for a detailed morphological study, and with sandbox modelling, the coupling of the craters can be elucidated.

### 3. Data acquisition and methods

#### 3.1. Landsat observations

To obtain a first impression of the architecture of the nested craters and the changes associated with the 1993 eruption, we examined Landsat data archives (Fig. 2). Landsat 7 (8 bands) and Landsat 8 (11 bands) feature data with a spatial resolution of 15–30 m. A qualitative and quantitative analysis of Landsat Thematic Mapper 7 data covering the 2000–2004 period, permitted the determination of the heat and mass flux through time (González et al., 2015) at Láscar. Landsat Thematic Mapper 5 was operational from 1984 to 2013, therefore including Láscar's 1993 eruption, and acquired data in seven spectral bands with a spatial resolution of 30 m. We created composite images existing of band 7 (red), band 4 (green) and band 3 (blue) covering the craters, using the ArcGIS software suite.

#### 3.2. TLS

Light Detecting And Ranging (LiDAR) remote sensing is based on the measurement of the time delay between the emission of a laser pulse and its reception upon reflection from the target object (Fornaciai et al., 2010). This way topographic details can be displayed covering large areas with great precision and in relatively little time. The LiDAR instrument can be mounted on aircraft for ALS or transported on the ground for TLS. To study structural and geomorphological features at the nested craters of Láscar, a ground-based LiDAR instrument was used.

We collected TLS data over two days in November 2013 using a long-range RIEGL LMS-Z620 Terrestrial Laser Scanner. For positioning, a Leica total station was used. In perfect conditions the laser scanner has a range of up to 2000 m (in clear atmosphere, a favourable viewing geometry and when the target has high reflectivity), a field of view of 80° by 360° in the vertical and horizontal plane, respectively, and a repeatability of up to 5 mm. We used reflectors, placed on (or 'behind') the scene, as tiepoints for co-registration and as Ground Control Points (GCPs) for georeferencing, and measured them using both the TLS and a total station. In total four TLS scans (a,b,c,d in Fig. 1d) were acquired, two from each viewpoint (1 and 2 in Fig. 1d), to overcome shadowing effects. The two point clouds from each view point were co-registered using the RiSCAN Pro Software (<http://www.riegl.com>) and then all data were combined into one point cloud, set in a local reference frame. These 'raw' LiDAR data allow investigation and quantification of the morphology of the nested craters of Láscar at cm-resolution.

#### 3.3. Analogue modelling

With analogue experiments we attempt to model the interaction between the craters after initial formation. As there are no evidences for shallow magma chambers at Láscar (Pritchard and Simons, 2002), and as the structural and generic mechanisms favour a funnel-type geometry (Matthews et al., 1997) our set-up differs from classic caldera experiments (e.g. Marti et al., 1994; Roche et al., 2000) in that we simulated the crater formation by a funnel mechanism. The experiments were conducted in a box of 60 cm by 45 cm by 10 cm. Three holes, with a diameter of 5 mm, were drilled in the bottom, with a spacing of 3.6 cm and 8.4 cm. These holes represent the conduits of the craters of Láscar, the distance between the holes was geometrically scaled to nature (see below for scaling details). We acknowledge conduits can also be elliptical or dyke-like (Tibaldi, 2015, and references therein), but to minimize the complexity of the modelled system, we do not consider that here. Most volcanoes, however, erupt through vents that are shaped like vertical cylinders (Burgisser and Degruyter, 2015). Furthermore TLS data reveals the almost circular outlines of the craters. The three holes could be

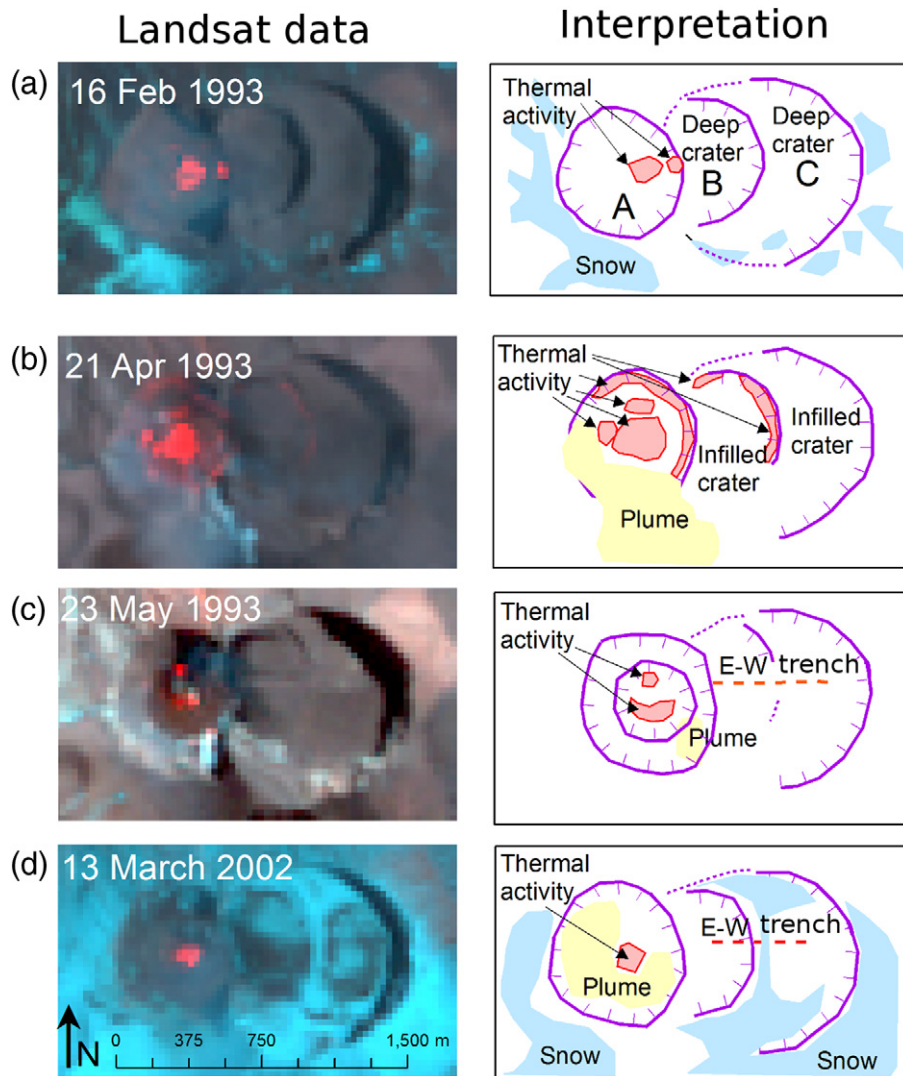


**Fig. 2.** Series of images acquired by the Landsat Thematic Mapper 5 satellite covering the 1993 eruption which had its main (VEI 4) explosion on the 18th of April. Showing the pre-eruptive (a), eruptive (b, c) and post-eruptive (d) activities. The different craters are depicted with A, B and C. Red colour shows the thermal band of the satellite in the Landsat data. See Section 4.1 Optical observations - Landsat for discussion.

opened or closed depending on the simulated scenario. The crater holes are firstly plugged and the box is filled to a depth of 8 cm with a granular material. Fine grained (<0.62 mm grain size), well-sorted sand is mixed at 1:20 by volume, with the same size black dyed sand, to facilitate camera observations, and at 1:10 by weight with plaster to increase the cohesion of the mixture.

Our analogue experiments follow the principle of similarity (Merle, 2015 and references therein) whereby lengths, material properties and deformation rates of the experiment scale to those in nature (Table 1). We choose a length ratio (geometric scaling factor)  $L^* = \frac{L_{\text{nature}}}{L_{\text{experiment}}} = 2 \times 10^{-5}$ , so that ~1 cm in the model corresponds to ~0.5 km in nature and the crater dimensions can be recreated in the lab. The density of most natural rocks lies between 2200–3000 kg/m<sup>3</sup>, twice as much as the analogue material density of 1260 kg/m<sup>3</sup> measured in the lab, meaning  $\rho^* = 0.5$ . The gravitational acceleration is equal in both model and nature, as the same gravitational conditions apply, thus  $g^* = 1$ . Therefore the dynamic scaling factor becomes  $\sigma^* = \rho^* \times g^* \times L^* = 10^{-5}$ . The cohesion of natural rocks ranges from  $10^2$ – $10^8$  Pa. When applying the stress scaling factor, the above natural cohesion range is scaled down by  $10^{-5}$ , meaning that the required analogue material cohesion should be 1 to  $10^3$  Pa. At

normal stresses applied in the models, cohesion of dry, fine-grained sand is 0 to 250 Pa. The cohesion of material, similar to the mixture we used, was measured to be  $65 \pm 80$  Pa, falling within this range and the angle of internal friction measured was  $0.71 \pm 0.01^\circ$  (personal communication Sam Poppe, August 2016).

For each experiment the sand/plaster mixture was sieved into the sandbox until a package with an approximate equal thickness of 8 cm was deposited. Craters A and C were formed by removing the plugs from the holes in the table ( $t=0$ ), allowing the mixture to flow out of the box, until a naturally stable slope for the material was reached. A little crest remained between the craters at depth (see Supplementary Fig. S1), but the general outline of these two craters at the surface was “nested”. Because these structures develop in accordance with the internal friction coefficient, only little shaking or vibration of the experiment table leads to further slumping and widening of the craters. The holes were closed by the plugs after reaching an equilibrium. This model was the starting condition for all other experiments ( $t=0$ ). The formed craters were then partly refilled with selected material ( $t=1$ ). The refill of the craters was done manually to accomplish a nearly complete overprinting, as observed at Láscaar Volcano during the 1993 eruption. We used

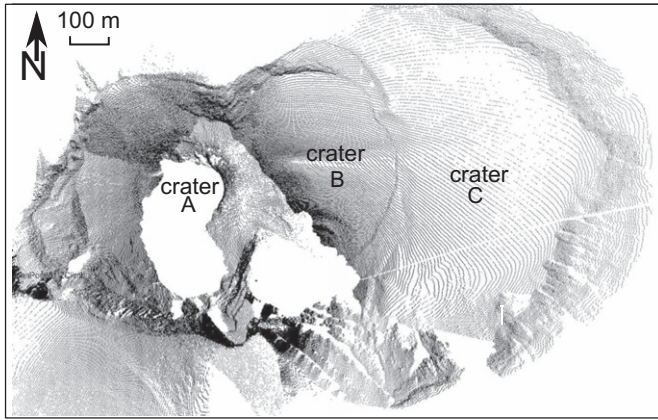


**Fig. 3.** TLS point cloud covering the three nested summit craters A, B and C of the edifice of Láscar Volcano. Crater A is the currently active crater from which explosions occur. See Section 4.2 TLS for discussion.

different materials for the refill, in order to simulate less cohesive or even ductile volcanic deposits. Glass beads are granular, sized 200–300  $\mu\text{m}$ , and have a near zero cohesion. Silicone putty with a viscosity of  $10^4$  Pa s was used to simulate gravitational spreading effects. The final step of each experiment was to remove the plug from crater A, and let the experiment run ( $t=2$ ) until a desired time. We examined the following processes: *i*) Formation of crater B due to continued subsidence in crater A, *ii*) Deformation in crater B and C due to variation in crater infill and continued subsidence in crater A (Supplementary Fig. S2a and b), and *iii*) Deformation in crater B and C due to pre-existing topography and continued subsidence in crater A (Supplementary Fig. S2c). During each experiment regular overhead photos were taken with a fixed camera and at the end of each time step oblique photos were taken using a hand-held camera.

## 4. Results

### 4.1. Optical observations - Landsat

Images acquired by the Landsat Thematic Mapper 5 satellite show the crater morphology before, during and after the April 1993 eruption (Fig. 2). The crater morphology of all three craters (A, B and C) is prominent before the main phase of the 1993 eruption, as seen in the image of 16 February 1993 (Fig. 2a). On 18 April 1993, the main phase of the eruption started and the extruded material smoothed, covered and in-filled large parts of the topography of crater B and C. Therefore, the nested crater structure becomes hidden beneath the eruption deposits. Crater outlines are concealed in the Landsat image of 21 April 1993 (Fig. 2b). The thermal band of the satellite, here depicted in red, shows crater A is highly active, as well as the rim of crater B. Shortly after the main phase of the 1993 eruption a linear E-W feature emerges, observable in the image of 23 May 1993

(Fig. 2c). Several years after the eruption, crater B stands out structurally in the Landsat image of 13 March 2002 (Fig. 2d). Together these observations indicate that the nested craters of Láscar have a long geologic history that has been present before and reactivated after the 1993 eruption. This indicates growth, subsidence and infill, but with a general geometric and structural arrangement that has not changed significantly over the past decades.

### 4.2. TLS

Accessibility prevented scanning from the northern rim of crater A. The white areas in the point cloud indicate areas of shadowing or areas that are otherwise beyond the reach of the scanner, so no data exists for these locations. The active crater (A in Fig. 3) is so deep that considering the angle and viewpoint of the laser no data points could be acquired of its floor and some of the steep crater walls. The darker areas in the point cloud implicate that the points have a dense sampling, resulting from overlap between the different scans and from improved backscatter close to the set-up location of the instrument. The combined point cloud has more than 15 million data points and an accuracy of about 20 cm in the local coordinate system (Fig. 3). The TLS data products are available for further use (Richter et al., 2016). We analyse the results from the TLS by generating a Digital Elevation Model (DEM), with 1-m pixel spacing, using the ArcGIS software. This is a great improvement compared to the DEM created by Pavez et al. (2006) which had a 10-m pixel spacing. We continue analysing the results by generating a slope map from the final point cloud (Fig. 4a), by creating a lineament map of the crater area (Fig. 4b), by Rose diagram statistics (Fig. 4c) and finally by drawing height profiles through several sections of the (DEM) (Fig. 5).

#### 4.2.1. Geomorphological findings

We use profiles through our point cloud to evaluate the diameter and depth of the craters in November 2013. The extend of all craters is fully covered. However, we can not entirely measure the depth of crater A and its depth is therefore a minimum estimate. We measure the diameter of the E-W and N-S axis of crater A, to be 650–800 m reaching a depth of at least 280 m. Similarly, crater B is 450–800 m across and 140 m deep relative to the highest part of the North rim. Crater C measures 1000–950 m across and is 210 m deep relative to the East rim. The crater floor of crater C is relatively flat, whereas the floor of crater B dips strongly (by  $25^\circ$  and 60–100 m) towards crater A (Fig. 5a).

#### 4.2.2. Structural findings

Two types of circumferential fractures can be observed in the point cloud (Fig. 3) and slope map (Fig. 4a), major crater rim fractures and smaller arcuate fractures. The slope map shows the steepness of the circumferential fractures bounding the craters. They can be traced for most of their circumferences, but are discontinuous for part of their length. We find the best-fit ellipsoids to express the outlines of the major crater rim fractures. The outlines of crater A can be described with an ellipse with an aspect ratio  $\frac{b}{a}=0.86$  and an azimuthal orientation of the long-axis of  $350^\circ$ . Crater B is defined by a distinct circumferential fracture on its northern and eastern side (numbered '2' in Fig. 4b) and can be fitted with an ellipse with an aspect ratio  $\frac{b}{a}=0.78$ , an orientation of the long-axis of  $350^\circ$  and a major-axis length of 450 m). The scarp of this circumferential fracture ranges from 4–20 m. A less obvious second ellipse can be fitted to the same crater, following the circumferential fracture 70 m further to the North (numbered '1' in Fig. 4b). This second ellipse has a major-axis length of 460 m, an aspect ratio of  $\frac{b}{a}=0.59$  and an orientation of the long-axis of  $350^\circ$ . This less distinct crater scarp ranges from 4–11 m. The circumferential fracture numbered '1' has been filled in more than the circumferential fracture numbered '2' and its average crater scarp is smaller than that of the other

**Table 1**  
Scaling values applied to the analogue experiments.

	Length	Density	Grav. acc.	Stress	Cohesion
	$L$	$\rho$	$g$	$\sigma$	$\tau$
	m	$\text{kg/m}^3$	$\text{m/s}^2$	Pa	Pa
Model	0.01	1260	$\sim 9.8$		$1-10^3$
Nature	500	2200–3000	$\sim 9.8$		$10^5-10^8$
Ratio	$2 \times 10^{-5}$	0.5	1	$1 \times 10^{-5}$	

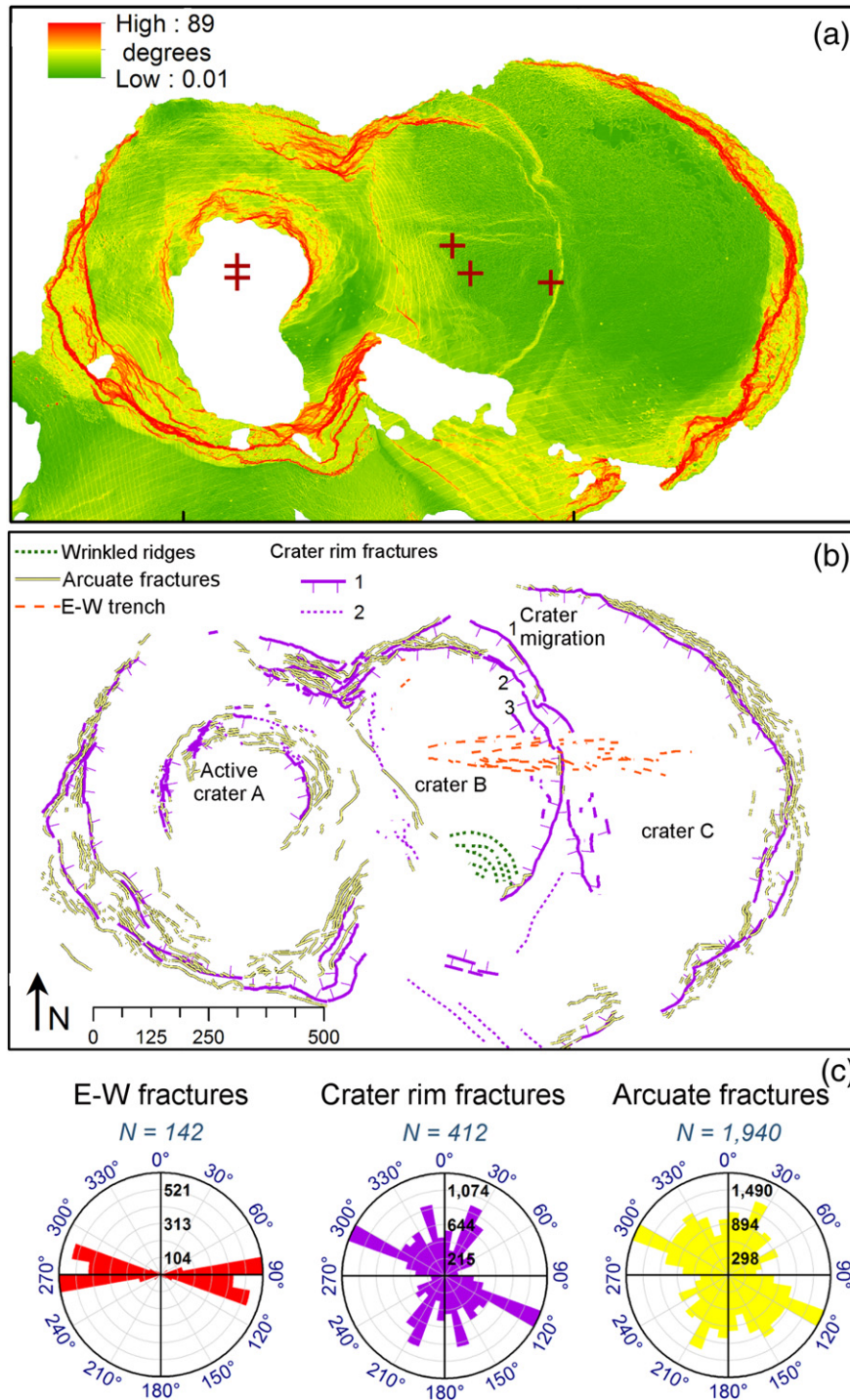


**Fig. 4.** a) Slope map generated from TLS, covering the 3 craters of the edifice of Láscaar Volcano. Red crosses show centres of best-fit ellipsoids to crater outlines. b) Lineament map generated from TLS slope map and point cloud. The following lineaments are depicted: crater rim fractures, E-W trench, arcuate fractures and wrinkled ridges. c) Rose diagrams calculated for each lineament category weighted by line length (black numbers). See text in Section 4.2 TLS for discussion.

fracture bounding crater B. We therefore suggest that the distinct crater scarp (numbered '2') is younger and more active. Crater C is outlined by crater rim fractures which can be fitted with a circle. We observe that the centres of the best fitting ellipsoids (for craters A and B) and circle (for crater C) are located on an E-W line (Fig. 4a).

The arcuate fractures are less pronounced than the crater rim fractures but follow their extension. They are located both in- and outside of the rim fractures. Crosscutting profiles show the scarp of

these fractures can be steep, from 5–60 m, dipping towards the crater centre. Each crater rim section consists of one or several of these down-dropped blocks. The November 2013 fieldwork confirmed active degassing occurs along some parts of these arcuate fractures.

Rose plots were created in ArcGIS (Jenness, 2014), and weighted according to length of the segments. The rose plot of the crater rim fractures (Fig. 4c) shows no preferred orientation but crater rim fractures with an azimuth from 120° are better developed. Similar

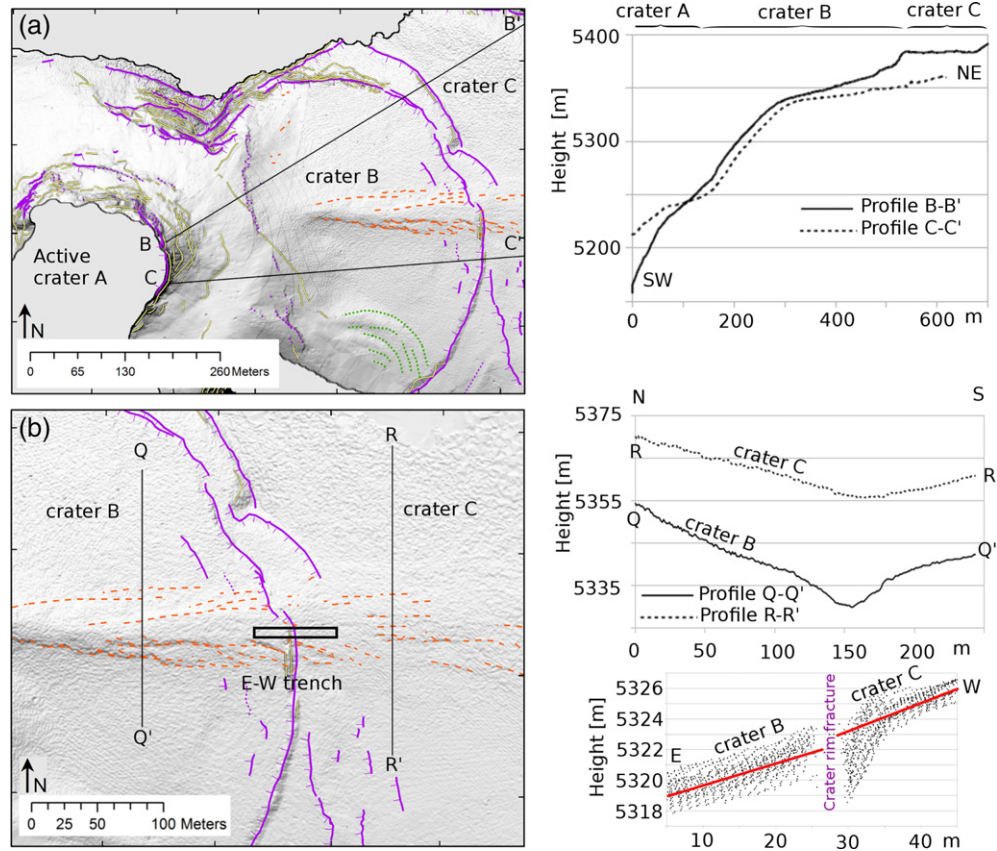


**Fig. 5.** a) Profiles through crater B, with the DEM in the background, are used to quantify the dip of crater B towards crater A. Crater rim fractures of crater B are clearly defined in the profile and visible as small steps. b) Profiles crosscutting the E-W trench show that i) the E-W trench extends into crater C, ii) the E-W trench forms a depression and iii) the E-W trench is more pronounced in crater B than in crater C. A stack of E-W profiles is taken from the area shown with a rectangle in the left hand panel. The stacked profiles (lower right hand panel) show a possible step of 1 m, crossing the crater rim fracture.

but less pronounced, the arcuate fractures are also better evolved at this azimuth. Most likely they represent fractures peripheral to the topographic rims of the craters with an extensional component. Such structures are commonly associated with recurrent gravitational slumping towards the crater centre (Lipman, 1997).

Other lineaments visible in the TLS data include the landslide feature in the South of crater B and an E-W lineament that is prominently visible in crater B but extends into crater C. Based on the fact that this lineament forms a depression, we refer to it as the “E-W trench” (Fig. 4b). The 850 m long E-W trench is defined by about fifty shorter structural segments varying in length from 20–200 m. The orientation of these segments falls into two discrete groups: N80–90°E or N100–110°E. Where the E-W trench is expected to crosscut the circumferential fractures of crater B, it locally aborts and recontinues at some distance to the East of the crossing. The arcuate fractures are all together absent in the area of crossing. The profiles perpendicular to the E-W trench (Fig. 5b) show it is pronounced and narrower on the East side (10 m wide, 10 m deep) and broadens out towards the West (140 m wide, 5 m deep).

#### 4.3. Analogue sandbox modelling

To improve our understanding of the interaction of the nested craters, sandbox craters A and C ( $t=0$  in Fig. 7a) were filled with glass beads topped with sand/plaster mixture ( $t=1$  in Fig. 7a), representing a low cohesion infill of the 1993 eruption as identified in the Landsat imagery. The experiment (Fig. 6, experiment set 1) shows that a structure, similar in size and outline to crater B, forms when

excavation of crater A continues (Fig. 7a). This result suggests that crater B may form and deepen by erosion and continued activity in crater A. We therefore consider this type of crater a ‘parasitic’ crater. To further test this concept, and also to elaborate if similar structures develop for a ductile crater infill, we repeated the experiment using a different infill material. When crater C was filled with silicone (Fig. 6, experiment set 2), a structure similar to crater B also develops, although less pronounced ring fractures form (Fig. 7b). We create a DEM of the end stage of each lab experiment using the Structure From Motion (SfM) technique applied to oblique photos using the Agisoft software. The similarity of the structure, comparable to crater B, that develops during both experiments, is evident from horizontal cross sections created from the DEMs (Fig. 7 bottom panels).

We compare the DEM generated from our TLS data to DEMs from the experiments (Fig. 8a). E-W profiles through the lab experiment DEMs (grey lines) compare well to an E-W profile through the TLS DEM (red line) (Fig. 8b). The prominent slope of the bottom of crater B, dipping towards crater A, is visible in both profiles. We also see similar outlines and similar slopes of crater A. Kinks in slope defining crater B are similarly expressed, although the exact position differs slightly in repeated experiment runs, depending on the infill material used. Crater C is flat in both, experiments and nature, indicating that it is largely inactive.

We test the influence of a variable crater infill on the deformation in crater B and C. We filled the ‘craters’ with different materials: glass beads, sand, sand/plaster mixture, silicone or alternating layers of several of these materials. We were able to recreate the

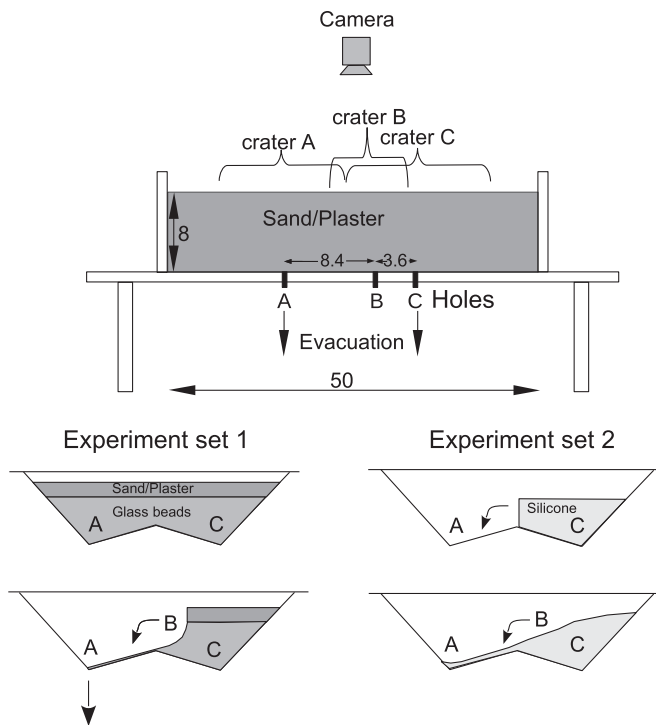


**Fig. 6.** Sketch of analogue experiment set-up, numbers in centimetres. Two ‘craters’ were formed in a 8 cm-thick sieved sand/plaster mixture (1:10 plaster by weight) by evacuation of material from the sandbox out of two holes in the bottom (A and C), which were 12 cm apart. The ‘craters’ were then filled with different materials during separate experiments (1 and 2). Finally the experiment was allowed to ‘run’ with or without opening the hole in the bottom of crater A.

crosscutting arcuate fractures seen in the northern area of crater B (Fig. 4b) when using an infill, from bottom to top, of glass beads, silicone and sand/plaster (Supplementary Fig. S2a). Another observation from these experiments is that when crater C is filled with a ductile material, such as a thin layer of silicone, excavation in crater A generates extension fractures close to the rim of crater C, parallel to the arcuate and rim fractures (Supplementary Fig. S2b). Deformation in crater A may thus be responsible for observed structures in crater C as well.

To study the deformation in crater B and C due to pre-existing topography, we filled crater C bowl-shaped rather than horizontally. In nature this could represent the enveloping of crater C with eruptive material from crater A. When adding a layer of silicone to these experiments, E-W orientated structures are formed with a folded relief (Supplementary Fig. S2c). These structures have a similar orientation to the E-W trench observed in nature. The difference being that in our experiments the E-W structures form a ‘hill’ by accumulating material and in nature the E-W trench forms a depression up to 10 m deep.

## 5. Discussion

From Landsat data we observe the crater morphology before, during and after the 1993 eruption. We find that the three nested craters were present before and after this eruption. During the eruption, volcanic products covered local structural features which gradually became visible again. This suggests that the structural features are active or reactivated, as was structurally and morphologically analysed by TLS data, and investigated in detail in analogue experiments.

### 5.1. Limitations

The resolution of the TLS data is unprecedented for Láscar (dense data sampling especially close to the scanner), however there are many data gaps in the data set. Despite these data gaps, it is possible to quantify observed features, such as crater depth, lineament lengths and fracture offsets. The TLS data have no temporal resolution and unfortunately no other DEM with similar resolution, to compare to, exists. This means our measurements show only one time step in the evolution of the craters of Láscar. Considering the small changes in morphology, even during larger eruptions, our data are however a solid basis for further studies.

Our structural interpretations are based on visibility of lineaments and verified in the field just from distance, as direct access to these structures is hazardous. Compared to previous interpretations of observed lineaments, we are now able to provide quantifications.

Analogue models are a simplification of nature but allow analysing specific and well selected parameters. Our models assume a funnel mechanism which could compare in nature to subsidence as a consequence of hydrothermal/degassing activity. We do not attempt to study how the craters formed initially, but rather focus on their interaction after formation.

We mainly use glass beads and silicone to simulate the deformable infill of the craters during the 1993 eruption. This is hypothetical, but a realistic scenario, as young eruption products may be thermally deformable or even ductile in their rheology. Both materials reproduce the general topography variation of the craters, although when using glass beads a more distinct crater B escarpment forms.

When simulating the way the infill material envelops the pre-existing topography, an E-W orientated structure forms. However, we fail to reproduce the well defined trench, comparable to nature. This suggests the process responsible for the E-W trench differs somewhat from the process mimicked in the analogue experiments, or that the initial geometry or conditions of our models are too simplified. Other processes such as cooling, erosion and compaction, which are not taken into account in our model, may play an important role in the formation of the E-W trench.

### 5.2. Interpretations

#### 5.2.1. Regional tectonic fingerprint

The Chilean Andes provide a natural laboratory to study the link between tectonics and magmatism (Cembrano and Lara, 2009; González et al., 2009). Several major composite andesitic volcanoes, within the CVZ, are spatially and genetically associated with the Pliocene-Pleistocene E-W shortening in the region (Cembrano and Lara, 2009). Large N-S trending depressions, the largest being the Salar de Atacama basin, form the boundary between the fore-arc and the arc along 22–26°S (González et al., 2009). Compressional faults are the major structural boundaries of these depressions. Composite volcanoes, such as Láscar, are spatially and temporally linked to the development of a Pliocene-Holocene N-S striking system of blind reverse faults and propagating folds (González et al., 2009). Such reverse faults have been mapped close to Láscar Volcano (Aron, 2008). E-W vertical fissures and/or dikes are consistent with E-W compression and might be the feeding mechanisms for emplacement of magma in this system (Aron et al., 2010). A prominent N-S-lineament, the Miscanti fault, crosscuts the Quaternary volcanic deposits (Zellmer et al., 2014) underlying the Láscar Volcano. González et al. (2009) suggest that the Miscanti fault (Fig. 1b), as observed South of the Láscar area, is the N-S trending hinge zone of an asymmetrical fault-propagated fold. Intersection of oblique-to-orthogonal fault systems (e.g., N-S-Miscanti and E-W-structures at Láscar) could facilitate and concentrate channels for magma extrusion. The regional tectonics may, in part, be responsible

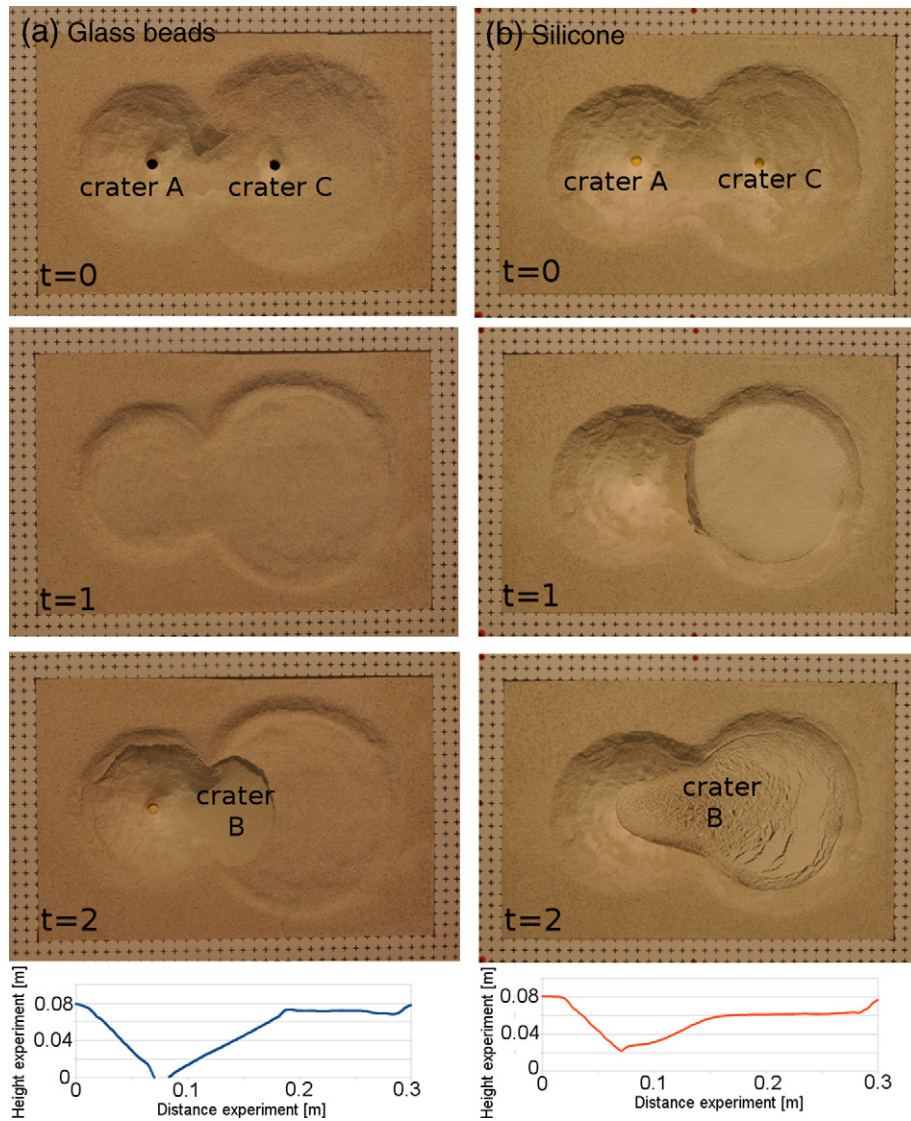


**Fig. 7.** Overhead analogue experiment photos displaying two end-members for the formation of crater B: glass beads and silicone filling of the craters. Background crosses have 1 cm spacing. At step 1 ( $t=0$ ) two craters are formed in the sandbox by opening of the holes in the bottom of craters A and C. During step 2 ( $t=1$ ), the craters are filled with glass beads topped with a thin layer of sand/plaster mixture (left panels) and with silicone dusted with plaster (right panel). During step 3 ( $t=2$ ), the experiments are allowed to run and we observe which structures form. The bottom panels show a horizontal cross section through the craters, created from the DEMs of the final stage of the two experiments.

for the E-W alignment of the craters of Láscaar but their exact relationship remains to be further studied.

### 5.2.2. Local interaction

A 1961 geological map of the area (Casertano et al., 1961) and aerial photographs of 1964 (Matthews et al., 1997 Fig. 2), already showed the craters in their present form. Matthews et al. (1997) described the depth and diameter of the summit craters: crater A has a diameter of 800 m and is 200–300 m deep, crater B is 600 m across and 100–200 m deep and crater C is 150–200 m deep and has a diameter of 1000 m. Assuming an original flat-topped surface, they implied a total minimum volume loss of approximately 0.2 km<sup>3</sup> for the three craters. Based on visual observations, Tassi et al. (2009) report crater A to be 400 m deep and 800 m across during the 2002–2006 period. Craters B and C endured no significant morphological changes during that period, crater A experienced subsidence of the crater floor related to the explosive activity in 2005 and 2006.

Based on the analogue experiments, we suggest crater B was formed as a parasitic structure, as a) a consequence of ongoing activity and excavation of material from crater A (Fig. 9a) and gravity driven slumping into that structure, or b) by compaction and sliding of the weak eruption infill into a pre-existing nested crater morphology (Fig. 9b). Both of these interpretations are in agreement with the glass beads and silicone experiments, respectively, forming very similar structures and nested architectures at the surface. We also show that an E-W orientated structure develops during some of the experiments. This suggests that a very local stress field may be responsible for the origin of the E-W trench.

In the past, activity at Láscaar has shifted from East to West and vice versa. In the last centuries activity seems to be shifting again towards the west side of the eastern edifice. We propose that the crater rim of crater B migrates towards the West, in the direction of crater A (see numbers 1, 2, and 3 in Fig. 4b). In this view, the degassing area in the East of crater B may become the location of a yet to form third circumferential fracture (number 3 in Fig. 4b). Further geodetic studies may more rigorously test this interpretation. We

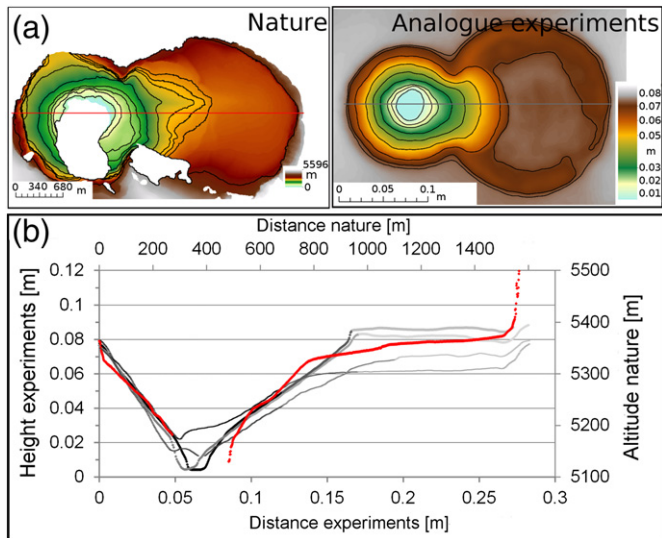
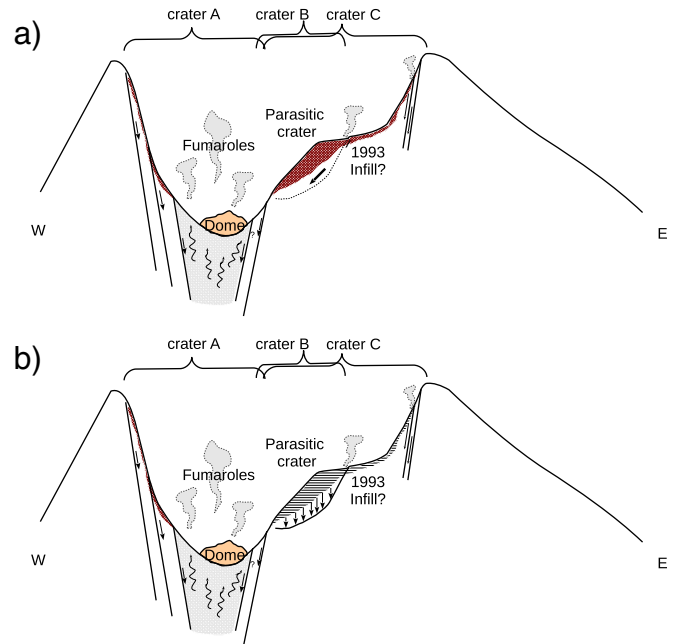


**Fig. 8.** a) Comparison of DEM generated from TLS data (nature) to DEM generated by SFM from oblique photos of the analogue experiment. Black lines show selected contour lines. Red and grey lines depict location of the profile shown below. b) Profiles through DEMs from analogue experiments (grey lines) compared to a profile through a DEM created from TLS data of Láscar Volcano (red line).

suggest, strengthened by analogue experiments, that crater B was not formed as a primal crater but rather as a parasitic feature, due to the activity in crater A. We study the crater rim fracture of crater B in more detail. A stack of E-W-profiles crosscutting the current site of biggest opening of this fracture (dashed rectangle in Fig. 4b) suggests a maximum possible step of 1 m. Therefore, the evolution and shaping of crater B is a still ongoing process. Furthermore, spreading and slumping into crater A may also induce deformation of crater C, as seen in for example the formation of extensional fractures around the crater C rim (Supplementary Fig. S2b). Even though in recent years only crater A has been erupting, its activity is the main factor responsible for the evolution of all the other craters of the edifice.

The last major (VEI 4) eruption of 1993 did not change the morphology of the craters extensively. To observe morphological changes caused by the 1993 eruption Pavez et al. (2006) show two aerial photographs of Láscar volcano, of 1981 and 1998 (their Fig. 2). Their 1981 photograph reveals the outlines of the craters similar to today. Their 1998 photograph shows only local changes, the most remarkable is the infill of all three craters and reactivation of their ring structures, and the other one is a N80°E oriented structure, which they assume to be a fracture and we refer to as the “E-W trench”. This linear feature, of uncertain origin, was first observed after the 1993 eruption by Matthews et al. (1997) and also documented in a picture from crater B taken in 1994 (Matthews et al., 1997 their Fig. 8). According to Matthews et al. (1997) the feature formed shortly after the 1993 eruption. Pavez et al. (2006) suggested it controlled permanent degassing during observations from 2002 to 2004, or even facilitated subsidence within crater B. The archived Landsat images covering the 1993 eruption, that we investigated (Fig. 2), also show the stable outlines of the craters and the appearance of the E-W trench after the initial eruption phase.

The E-W trench can be observed in all aerial photographs (Gardeweg et al., 1998; Jessop et al., 2012; Pavez et al., 2006), field photos (Matthews et al., 1997) and satellite images (Murphy et al., 2010) acquired after the 1993 eruption. This suggests the E-W trench was formed in relation to the 1993 eruption or became prominent shortly after the 1993 eruption. The lineament is unmistakable in our



**Supplementary Fig. 2.** Overhead analogue experiment photos displaying three different experiment runs done to study varying processes. Background crosses have 1 cm spacing. At step 1 ( $t=0$ ) two craters are formed in the sandbox by opening of the holes in the bottom of craters A and C. During step 2 ( $t=1$ ), the craters are filled with a layer of glass beads, followed by a thin layer of silicone and topped of by a layer of sand/plaster mixture. In a) and b) these layers are positioned horizontally while in c) these layers are bowl-shaped following the topography of the craters. During step 3 ( $t=2$ ), the experiments are allowed to run and we observe which structures form. The bottom panels show a close up of the structures of interest.

TLS data and covers not only crater B, but also continues into crater C (Fig. 5a). The E-W trench forms the centre of the valley shaped depression of crater B and C and does not seem to have a different lithology compared to its surroundings. It currently displays small amounts of degassing mainly in crater C, but no tensile fractures are visible along its exposure, and no clear lateral shear indicators are displayed.

Although we were able to produce an E-W orientated structure in some of our analogue models, suggesting a local stress field may be responsible for its formation, the exact origin of the E-W trench remains ambiguous. Other possibilities include a dyke, a fracture or simply a redistribution of the eruption infill forming a ‘through’. The direction of maximum horizontal stress, in the local compressive stress regime (regional stress field) at Láscar, is roughly E-W (Aron, 2008), with possible dyke(s) forming parallel to this. Tibaldi (2015, and references therein) explains the relation between shallow magma emplacement and local surface deformation, taking into account the possibility of a dyke beneath a zone of subsidence. They suggest two models for the deformation of the surface topography above a shallow propagating dyke tip: (1) Uplift zones on each side of the dyke tip and no uplift above the dyke tip itself, with propagation of normal faults and fissures at the surface. (2) Uplift of the zone above the dyke tip with propagation of reverse faults and fissures at the surface. Neither of these models can be applied to the E-W trench observed at Láscar as only a depression is observed there. Furthermore, crosscutting relationships indicate marginal activity of the E-W trench. Finally, no dyke traces have been observed in the field on any of the crater walls, making the existence of a single buried dyke unlikely. If the E-W trench was the surface expression of a fracture, we would expect it to be a tensional fracture, in line with the local stress regime. We do not observe any evidence in the field for a tensional fracture, such as visible opening and a raised surface at the crest of the fracture. The E-W trench may have formed due to

volume change or redistribution of material shortly after the 1993 eruption. This also resulted in sagging and spreading of the floors of crater B and C, possibly forming a ‘through’ in the middle which can be observed as an E-W trench. The redistribution of material was focussed towards crater A, as we have shown in experiments, which results in a more prominent ‘through’ closer to this crater and a general plunge of the ‘through’ towards the West. Our models consider a lateral spreading and slumping process, but do not consider redistribution of the infilling material. Redistribution could be due to cooling and/or compaction of erupted material as well as gravitational sliding. This is our favourite interpretation of the origin of the E-W trench, as it does not contradict any of the observations but this needs to be subject of further investigation.

### 5.3. Implications

We compare the summit craters of Láscar to other volcanoes with nested craters or calderas as these may also exhibit similar evolution mechanisms. Masaya in Nicaragua is a large basaltic shield volcano which developed a suite of nested calderas and craters. Rymer et al. (1998) suggest the pit craters of Masaya Volcano form during cycles of intense degassing, lava lake development and collapse along outward-dipping faults surrounding the pit craters as well as by incremental collapse of caverns formed within the boundaries of the pit craters. At a much larger scale Belousov et al. (2005), reported how the shape of a caldera depends on the pre-caldera topography, and how pre-caldera stratocones react when caldera’s form. The common mechanism used to explain overlapping calderas, such as at Tenerife (Martí and Gudmundsson, 2000), is by migration of the associated magma chamber. Here, we have proposed a completely different mechanism for the formation of one of the nested summit craters of Láscar. Crater B formed as a ‘parasite’ crater, due to gravitational sliding towards the active crater A (Fig. 9a). Such secondary features have been described at a much larger scale (Karatson et al., 1999). Merle and Lénat (2003) have used analogue models to explain the formation of a pseudo caldera at Piton de la Fournaise (La Reunion) and have suggested similar processes may be active at Fogo (Cape Verde Islands) and Las Cañadas (Canary Islands). The concept of parasite craters and pseudo calderas is likely applicable to other volcanoes worldwide and bears similarities to the scenario considered by us for Láscar Volcano.

## 6. Conclusion

We study the enigma of the nested craters of Láscar Volcano. Landsat data suggest that the nested crater architecture was reactivated after the 1993 eruption. Using TLS we are able to analyse and quantify the topography and geomorphological structures in unprecedented detail. We compare the data to analogue models and learn that the central crater (B) may actually be a ‘parasite’ crater. We suggest that initially only crater A and C were formed, and as activity continued in crater A, a secondary crater (B) developed in between crater A and C, due to gravitational slumping of material towards crater A. This concept of a ‘parasite’ crater is likely applicable to other volcanoes elsewhere.

### Acknowledgments

This work (EDZ and NR) was supported by the Helmholtz Alliance Remote Sensing and Earth System Dynamics (HGF EDA). TW received financial support from TOPOMOD and VOLCAPSE (ERC-COG 646858). Fieldwork was financed by GFZ. We thank Mehdi Nikkhou for his help with the data collection, the data processing and for the many valuable discussions which greatly improved the paper. We thank M. Zimmer, C. Kujawa, J. Salzer and M. Leonhardt for their help during field work. Access to the RIEGL

instrument was kindly provided by the University of Potsdam and supported by A. Landgraf. A Geotiff of the DEM is available on-line at <http://dx.doi.org/10.5880/GFZ.2.1.2016.002>. We thank our colleagues at the GFZ section Physics of Earthquakes and Volcanoes, especially E. Holohan, for valuable suggestions which enhanced the manuscript. We thank O. Oncken and M. Rosenau for providing access to the analogue modelling lab and F. Neumann for assistance in the lab. Constructive reviews by A. Geyer and A. Tibaldi greatly improved the manuscript.

### Appendix A. Supplementary data

Supplementary data to this article can be found online at <http://dx.doi.org/10.1016/j.jvolgeores.2016.09.018>.

## References

- Acocella, V., 2008. Activating and reactivating pairs of nested collapses during caldera-forming eruptions: Campi Flegrei (Italy). *Geophys. Res. Lett.* 35 (17). <http://dx.doi.org/10.1029/2008GL035078>. L17,304.
- Acocella, V., Cifelli, F., Funicello, R., 2001. Formation of non-intersecting nested calderas: insights from analogue models. *Terra Nova* 13 (1), 58–63. <http://dx.doi.org/10.1046/j.1365-3121.2001.00317.x>.
- Aron, F., 2008. *Arquitectura y estilo de la deformación compresiva neógena del borde sur-oriental del Salar de Atacama, Norte de Chile (23° 30' sur): su relación con el volcanismo Plio-Cuaternario de los Andes Centrales*. Universidad católica del Norte, Facultad de Ingeniería y Ciencias Geológicas, Departamento de Ciencias Geológicas. (Ph.D. thesis)
- Aron, F.A., González, G., Cembrano, J.M., Veloso, E.E., 2010. Reverse faulting as a crucial mechanism for magma ascent in compressional volcanic arcs: field examples from the central andes. *American Geophysical Union, Fall Meeting*. (V43B-2379).
- Belousov, A., Walter, T.R., Troll, V.R., 2005. Large-scale failures on domes and stratocones situated on caldera ring faults: sand-box modeling of natural examples from Kamchatka, Russia. *Bull. Volcanol.* 67, 457–468. <http://dx.doi.org/10.1007/s00445-004-0387-1>.
- Branney, M., 1995. Downsag and extension at calderas: new perspectives on collapse geometries from ice-melt, mining, and volcanic subsidence. *Bull. Volcanol.* 57 (5), 303–318. <http://dx.doi.org/10.1007/BF00301290>.
- Burgisser, A., Degruyter, W., 2015. Magma ascent and degassing at shallow levels. In: Sigurdsson, H., Houghton, B., McNutt, S.R., Rymer, H., Stix, J. (Eds.), *The Encyclopedia of Volcanoes*, second edition. Elsevier, London, San Diego, Waltham, Oxford, pp. 225–236.
- Calder, E.S., Sparks, R.S.J., Gardeweg, M.C., 2000. Erosion, transport and segregation of pumice and lithic clasts in pyroclastic flows inferred from ignimbrite at Láscar Volcano, Chile. *J. Volcanol. Geotherm. Res.* 104, 201–235. [http://dx.doi.org/10.1016/S0377-0273\(00\)00207-9](http://dx.doi.org/10.1016/S0377-0273(00)00207-9).
- Casertano, L., Barozzi, R., Lomnitz, C., Garin, J., 1961. Informe sobre el sistema volcánico del Láscar. Apartado 18 de los Anales de la Facultad de Ciencias Físicas y Matemáticas de la Universidad de Chile, Publicación N°. 23. Universidad de Chile, Instituto de Geología, pp. 305–318.
- Cembrano, J., Lara, L., 2009. The link between volcanism and tectonics in the southern volcanic zone of the Chilean Andes: a review. *Tectonophysics* 471, 96–113. <http://dx.doi.org/10.1016/j.tecto.2009.02.038>.
- Corazzato, C., Tibaldi, A., 2006. Fracture control on type, morphology and distribution of parasitic volcanic cones: an example from Mt. Etna, Italy. *J. Volcanol. Geotherm. Res.* 158, 177–194.
- de Silva, S.L., 1989. Altiplano-Puna volcanic complex of the Central Andes. *Geology* 17, 1102–1106. [http://dx.doi.org/10.1130/0091-7613\(1989\)017](http://dx.doi.org/10.1130/0091-7613(1989)017).
- de Silva, S.L., Zandt, G., Trumbull, R., Viamonte, J.G., Salas, G., Jimenez, N., 2006. Large ignimbrite eruptions and volcano-tectonic depressions in the Central Andes: a thermomechanical perspective. In: Troise, C., de Natale, G., Kilburn, C. (Eds.), *Mechanisms of Activity and Unrest at Large Calderas*, Special publications. vol. 269. Geological Society, London, pp. 47–63.
- Denniss, A.M., Harris, A.J.L., Rothery, D.A., Francis, P.W., Carlton, R.W., 1998. Satellite observations of the April 1993 eruption of Láscar volcano. *Int. J. Remote Sens.* 19 (5), 801–821. <http://dx.doi.org/10.1080/014311698215739>.
- Díaz, D., Brasse, H., Ticona, F., 2012. Conductivity distribution beneath Láscar volcano (Northern Chile) and the Puna, inferred from magnetotelluric data. *J. Volcanol. Geotherm. Res.* 217, 21–29. <http://dx.doi.org/10.1016/j.jvolgeores.2011.12.007>.
- Fornaciai, A., Bisson, M., Landi, P., Mazzarini, F., Pareschi, M.T., 2010. A LiDAR survey of Stromboli volcano (Italy): digital elevation model-based geomorphology and intensity analysis. *Int. J. Remote Sens.* 31 (12), 3177–3194. <http://dx.doi.org/10.1080/01431160903154416>.
- Francis, P.W., de Silva, S.L., 1989. Application of the Landsat Thematic Mapper to the identification of potentially active volcanoes in the Central Andes. *Remote Sens. Environ.* 28, 245–255. [http://dx.doi.org/10.1016/0034-4257\(89\)90117-X](http://dx.doi.org/10.1016/0034-4257(89)90117-X).
- Gardeweg, M.C., Sparks, R.S.J., Matthews, S.J., 1998. Evolution of Láscar volcano, Northern Chile. *J. Geol. Soc.* 155 (1), 84–104. <http://dx.doi.org/10.1144/gsjgs.155.1.0089>.
- Geyer, A., García-Sellés, D., Pedrazzi, D., Barde-Cabusson, S., Martí, J., Muñoz, J., 2015.

- Studying monogenetic volcanoes with a terrestrial laser scanner: case study at croscat volcano (Garrotxa Volcanic Field, Spain). *Bull. Volcanol.* 77 (3), 1–14. <http://dx.doi.org/10.1007/s00445-015-0909-z>.
- Glaze, L.S., Francis, P.W., Rothery, D.A., 1989. The 16 September 1986 eruption of Láscar volcano, North Chile: satellite investigations. *Bull. Volcanol.* 51 (3), 149–160. <http://dx.doi.org/10.1007/BF01067952>.
- González, C., Inostroza, M., Aguilera, F., González, R., Viramonte, J., Menzies, A., 2015. Aug. Heat and mass flux measurements using Landsat images from the 2000–2004 period, Láscar volcano, northern Chile. *J. Volcanol. Geotherm. Res.* 301, 277–292. <http://dx.doi.org/10.1016/j.jvolgeores.2015.05.009>.
- González, G., Cembrano, J., Aron, F., Veloso, E.E., Shyu, J.B.H., 2009. Coeval compressional deformation and volcanism in the Central Andes, case studies from Northern Chile (23S24S). *Tectonics* 28 (TC6003). <http://dx.doi.org/10.1029/2009TC002538>.
- Holohan, E., Schöpfer, M., Walsh, J., 2011. Mechanical and geometric controls on the structural evolution of pit crater and caldera subsidence. *J. Geophys. Res.* 116 (B7), B07202, <http://dx.doi.org/10.1029/2010JB008032>.
- Holohan, E.P., van Wyk de Vriess, B., Troll, V.R., 2008. Analogue models of caldera collapse in strike-slip tectonic regimes. *Bull. Volcanol.* 70, 773–796. <http://dx.doi.org/10.1007/s00445-007-0166-x>.
- Jagger, T., 1947. Origin and development of craters. *Geol. Soc. Am. Mem.* 21, 1–586. <http://dx.doi.org/10.1130/MEM21-p1>.
- James, M.R., Pinkerton, H., Applegarth, L.J., 2009. Detecting the development of active lava flow fields with a very-long-range terrestrial laser scanner and thermal imagery. *Geophys. Res. Lett.* 36, L22305 <http://dx.doi.org/10.1029/2009GL040701>.
- Jenness, J., 2014. *Polar Plots and Circular Statistics: Extension for ArcGIS*. Jenness Enterprises.
- Jessop, M.C., Kelfoun, R.S.J., Labazuy, S.J., Roche, S.J., Trouillet, S.J., Thibault, S.J., 2012. LiDAR derived morphology of the 1993 Láscar pyroclastic flow deposits, and implication for flow dynamics and rheology. *J. Volcanol. Geotherm. Res.* 97, 81–104. <http://dx.doi.org/10.1016/j.jvolgeores.2012.06.030>.
- Jones, L.K., Kyle, P.R., Oppenheimer, C., Frechette, J.D., Okal, M.H., 2015. Terrestrial laser scanning observations of geomorphic changes and varying lava lake levels at Erebus volcano, Antarctica. *J. Volcanol. Geotherm. Res.* 295, 43–54. <http://dx.doi.org/10.1016/j.jvolgeores.2015.02.011>.
- Jones, R.R., Kokkalas, S., McCaffrey, K.J.W., 2009. Quantitative analysis and visualization of nonplanar fault surfaces using terrestrial laser scanning (LIDAR)-the Arkitisa Fault, central Greece, as a case study. *Geosphere* 5 (6), 465–482. <http://dx.doi.org/10.1130/GES00216.1>.
- Karatson, D., Thouret, J.-C., Moriya, I., Lomoschitz, A., 1999. Erosion calderas: origins, processes, structural and climatic control. *Bull. Volcanol.* 61 (3), 174–193. <http://dx.doi.org/10.1007/s004450050270>.
- Kennedy, B.M., Jellinek, A.M., Stix, J., 2008. Coupled caldera subsidence and stirring inferred from analogue models. *Nat. Geosci.* 1, 385–389. <http://dx.doi.org/10.1038/ngeo206>.
- Komuro, H., 1987. Experiments on cauldron formation: a polygonal cauldron and ring fractures. *J. Volcanol. Geotherm. Res.* 31 (87), 139–149. [http://dx.doi.org/10.1016/0377-0273\(87\)90011-4](http://dx.doi.org/10.1016/0377-0273(87)90011-4).
- LaFemina, P., Hudak, M., Feineman, M., Geirsson, H., Normandeau, J., Furman, T., 2015. Inside the volcano: the how and why of Thrihnukagigur volcano, Iceland. *Geophys. Res. Abstr.* 17, EGU2015-9498.
- Lipman, P., 2000. Calderas. In: Sigurdsson, H. (Ed.), *Encyclopedia of Volcanoes*. Academic Press, San Francisco, pp. 643–662.
- Lipman, P.W., 1997. Subsidence of ash-flow calderas: relation to caldera size and magma-chamber geometry. *Bull. Volcanol.* 59, 198–218. <http://dx.doi.org/10.1007/s004450050186>.
- Lockwood, J.P., 1990. Implications of historical eruptive vent migration on the northeast rift zone of Mauna Loa Volcano, Hawaii. *Geology* 15 (7), 611–613. <http://dx.doi.org/10.1130/0091-7613>.
- Marti, J., Ablay, G.J., Redshaw, L.T., Sparks, R.S.J., 1994. Experimental studies of collapse calderas. *J. Geol. Soc.* 151, 919–929. <http://dx.doi.org/10.1144/gsjgs.151.6.0919>.
- Marti, J., Gudmundsson, A., 2000. The Las Cañadas caldera (Tenerife, Canary Islands): an overlapping collapse caldera generated by magma-chamber migration. *J. Volcanol. Geotherm. Res.* 103, 161–173. [http://dx.doi.org/10.1016/S0377-0273\(00\)00221-3](http://dx.doi.org/10.1016/S0377-0273(00)00221-3).
- Matthews, S.J., Gardeweg, M.C., Sparks, R.S.J., 1997. The 1984 to 1996 cyclic activity of Láscar volcano, Northern Chile: cycles of dome growth, dome subsidence, degassing and explosive eruptions. *Bull. Volcanol.* 59 (1), 72–82. <http://dx.doi.org/10.1007/s004450050176>.
- Merle, O., 2015. The scaling of experiments on volcanic systems. *Front. Earth Sci.* 3 (26). <http://dx.doi.org/10.3389/feart.2015.00026>.
- Merle, O., Lénat, J.-F., 2003. Hybrid collapse mechanism at Piton de la Fournaise volcano, Reunion Island, Indian Ocean. *J. Geophys. Res. Solid Earth* 108 (B3), 2156–2202. <http://dx.doi.org/10.1029/2002JB002014>.
- Murphy, S.W., de Souza Filho, C.R., Oppenheimer, C., 2010. The spatial extent of thermal anomalies at Láscar volcano. *IEEE International Symposium on Geoscience and Remote Sensing IGARSS*, pp. 1557–1560. *Proceedings Paper*. <http://dx.doi.org/10.1109/IGARSS.2010.5652858>.
- Oppenheimer, C., Francis, P., Rothery, D., Carlton, R., 1993. Infrared image analysis of volcanic thermal features: Láscar volcano, Chile, 1984–1992. *J. Geophys. Res.* 98 (B3), 4269–4286. <http://dx.doi.org/10.1029/92JB02134>.
- Pavez, A., Remy, D., Bonvalat, S., Diament, M., Gabalda, G., Froger, J., Julien, P., Legrand, D., Moisset, D., 2006. Insight into ground deformations at Láscar volcano (Chile) from SAR interferometry, photogrammetry and GPS data: implications on volcano dynamics and future space monitoring. *Remote Sens. Environ.* 100 (3), 307–320. <http://dx.doi.org/10.1016/j.rse.2005.10.013>.
- Pesci, A., Teza, G., Casula, G., Loddio, F., De Martino, P., Dolce, M., Obrizzo, F., Pingue, F., 2011. Multitemporal laser scanner-based observation of the Mt. Vesuvius crater: characterization of overall geometry and recognition of landslide events. *ISPRS J. Photogramm. Remote Sens.* 66 (3), 327–336. <http://dx.doi.org/10.1016/j.isprsjprs.2010.12.002>.
- Pesci, A., Teza, G., Casula, G., Fabris, M., Bonforte, A., 2013. Remote sensing and geodetic measurements for volcanic slope monitoring: surface variations measured at Northern flank of La Fossa Cone (Vulcano island, Italy). *Remote Sens.* 5 (5), 2238–2256. <http://dx.doi.org/10.3390/rs5052238>.
- Poppe, S., Holohan, E.P., Pauwels, E., Cnudde, V., Kervyn, M., 2014. Sinkholes, pit craters, and small calderas: analog models of depletion-induced collapse analyzed by computed X-ray microtomography. *Geol. Soc. Am. Bull.* 127 (1–2), 281–296. <http://dx.doi.org/10.1130/B30989.1>.
- Pritchard, M.E., Simons, M., 2002. A satellite geodetic survey of large-scale deformation of volcanic centres in the Central Andes. *Nature* 418 (6894), 167–171. <http://dx.doi.org/10.1038/nature00872>.
- Pritchard, M.E., Simons, M., 2004. An InSAR-based survey of volcanic deformation in the Central Andes. *Geochem. Geophys. Geosyst.* 31, L15610, <http://dx.doi.org/10.1029/2003GC000610>.
- Richter, N., Nikkhoo, M., de Zeeuw-van Dalfsen, E., Salzer, J., Walter, T. R., 2016. Terrestrial laser scanner data covering the summit craters of Láscar Volcano, Chile. *GFZ Data Services* <http://dx.doi.org/10.5880/GFZ.2.1.2016.002>.
- Roche, O., Druitt, T.H., Merle, O., 2000. Experimental study of caldera formation. *J. Geophys. Res.* 105 (B1), 395–416. <http://dx.doi.org/10.1029/1999JB900298>.
- Roche, O., van Wyk de Vries, B., Druitt, T.H., 2001. Sub-surface structure and collapse mechanisms of summit pit craters. *J. Volcanol. Geotherm. Res.* 105, 1–18. [http://dx.doi.org/10.1016/S0377-0273\(00\)00248-1](http://dx.doi.org/10.1016/S0377-0273(00)00248-1).
- Rymer, H., van Wyk de Vries, B., Stix, J., Williams-Jones, G., 1998. Pit crater structure and processes governing persistent active craters Masaya Volcano, Nicaragua. *Bull. Volcanol.* 59, 345–355. <http://dx.doi.org/10.1007/s004450050196>.
- Scolamacchia, T., Pullinger, C., Caballero, L., Montalvo, F., Orosco, L.E.B., Hernandez, G.G., 2010. The 2005 eruption of Ilamatepec (Santa Ana) volcano, El Salvador. *J. Volcanol. Geotherm. Res.* 189 (34), 291–318. <http://dx.doi.org/10.1016/j.jvolgeores.2009.11.016>.
- Sparks, R.S.J., Gardeweg, M.C., Calder, E.S., Matthews, S.J., 1997. Erosion by pyroclastic flows on Láscar volcano, Chile. *Bull. Volcanol.* 58, 557–565. <http://dx.doi.org/10.1007/s004450050162>.
- Tassi, F., Aguilera, F., Vaselli, O., Medina, E., Tedesco, D., Delgado Huertas, A., Poreda, R., Kojima, S., 2009. The magmatic- and hydrothermal-dominated fumarolic system at the active crater of Láscar volcano, Northern Chile. *Bull. Volcanol.* 71 (2), 171–183. <http://dx.doi.org/10.1007/s00445-008-0216-z>.
- Thouret, J.-C., Finizola, A., Fornari, M., Legey-Padovani, A., Suni, J., Frechen, M., 2001. Geology of El Misti volcano near the city of Arequipa, Peru. *Geol. Soc. Am. Bull.* 113 (12), 1593–1610. <http://dx.doi.org/10.1130/0016-7606>.
- Tibaldi, A., 2015. Structure of volcano plumbing systems: a review of multi-parametric effects. *J. Volcanol. Geotherm. Res.* 298, 85–135. <http://dx.doi.org/10.1016/j.jvolgeores.2015.03.023>.
- Valentine, G.A., White, J.D.L., Ross, P.-S., Amin, J., Taddeucci, J., Sonder, I., Johnson, P.J., 2012. Experimental craters formed by single and multiple buried explosions and implications for volcanic craters with emphasis on maars. *Geophys. Res. Lett.* 39 (20). <http://dx.doi.org/10.1029/2012gl053716>.
- Walter, T.R., Troll, V.R., 2001. Formation of caldera periphery faults: an experimental study. *Bull. Volcanol.* 63, 191–203. <http://dx.doi.org/10.1007/s004450100135>.
- Zellmer, G.F., Freymuth, H., Cembrano, J.M., Clavero, J.E., Veloso, E.A.E., Sielfeld, G.G., 2014. Orogenic Andesites and Crustal Growth, chap. Altered mineral uptake into fresh arc magmas: insights from U Th isotopes of samples from Andean volcanoes under differential crustal stress regimes. *Geological Society, London, Special Publications* 385, pp. 185–208. <http://dx.doi.org/10.1144/SP385.9>.